



Electrolyte design for LiF-rich solid-electrolyte interfaces to enable high-performance micro-sized alloy anodes for batteries

Ji Chen^{1,8}, Xiulin Fan^{1,8}, Qin Li^{1,8}, Hongbin Yang², M. Reza Khoshi³, Yaobin Xu⁴, Sooyeon Hwang⁵, Long Chen¹, Xiao Ji¹, Chongyin Yang¹, Huixin He³, Chongmin Wang⁴, Eric Garfunkel², Dong Su⁵, Oleg Borodin⁶✉ and Chunsheng Wang^{1,7}✉

Lithium batteries with Si, Al or Bi micro-sized (>10 μm) particle anodes promise a high capacity, ease of production, low cost and low environmental impact, yet they suffer from fast degradation and a low Coulombic efficiency. Here we demonstrate that a rationally designed electrolyte (2.0 M LiPF₆ in 1:1 v/v mixture of tetrahydrofuran and 2-methyltetrahydrofuran) enables 100 cycles of full cells that contain micro-sized Si, Al and Bi anodes with commercial LiFePO₄ and LiNi_{0.8}Co_{0.15}Al_{0.05}O₂ cathodes. Alloy anodes with areal capacities of more than 2.5 mAh cm⁻² achieved >300 cycles with a high initial Coulombic efficiency of >90% and average Coulombic efficiency of >99.9%. These improvements are facilitated by the formation of a high-modulus LiF-organic bilayer interphase, in which LiF possesses a high interfacial energy with the alloy anode to accommodate plastic deformation of the lithiated alloy during cycling. This work provides a simple yet practical solution to current battery technology without any binder modification or special fabrication methods.

Alloys such as Li_xSi, Li_xAl and Li_xBi are among the most promising anode materials for Li-ion batteries (LIBs) due to their high theoretical capacities¹. Large (>10 μm) Si, Al or Bi microparticles (SiMPs, AlMPs or BiMPs, respectively) are attractive due to their low production cost and high tap density. However, a large volume expansion during battery operation leads to the mechanical fracture of particles, which induces a loss of active material and exposes the highly reactive surface to the electrolyte. This leads to a continuous growth of the solid-electrolyte interphase (SEI), electrolyte consumption, low cycling Coulombic efficiency (CE) and poor cycle life. Organic-inorganic SEIs formed in traditional carbonate electrolytes are not robust enough to accommodate the volume expansion of SiMPs, AlMPs and BiMPs (up to 280%). Consequently, SiMP, AlMP and BiMP anodes exhibit a fast capacity drop, typically a retention of <60% in 20 charge/discharge cycles².

Owing to the limited success in improving micro-sized Si electrode performances by optimizing the electrode fabrication^{3,4} and cycling conditions⁵, attention turned to Si nanoengineering. Nanosized Si particles and Si wires show an improved resistance to fracture during (de)lithiation cycles^{6,7}. One-dimensional nanowires⁸, core-shell nanostructures^{9,10}, hollow particles¹¹, tubes¹², porous Si (ref. ¹³), silicon carbide (SiC)^{14,15} and SiC/MXenes¹⁶ improve the cycling stability in half-cells. However, the complex fabrication, high cost, low tap density and initial CE make these approaches unsuitable for practical applications. Functional binders with self-healing and elastic properties kept the pulverized SiMPs coalesced without disintegration^{17–20}, which enabled 1–3 μm SiMPs to be charged/discharged in a half-cell for 150 cycles with an initial CE of 91% and average cycling

CE of 99.6%, and in a Si/LiNi_{0.8}Co_{0.15}Al_{0.05}O₂ (NCA) full cell for 50 cycles¹⁸. Encapsulating 1–3 μm SiMPs with a conformal multilayered graphene cage allows the SiMPs to expand and fracture within the cage, with the electrolyte blocked by a stable SEI formed on the graphene cage surface¹⁹. The graphene-encapsulated SiMPs exhibit an initial CE of 93.2%, which increases to 99.5% after five cycles²¹. However, the relatively low average cycling CE of <99.6% for Si (99.9% is needed for practical applications; Supplementary Fig. 1) requires a substantial excess of Li to be introduced either by a costly prelithiation step or by using oversized cathodes, which increases the cost or reduces the battery energy density.

Many electrolytes and additives were also developed to further improve the cycling CEs, but the lack of a SEI design principle for alloying anodes hinders success. Carbonate electrolytes with fluoroethylene carbonate (FEC) and/or vinylene carbonate additives yield the best performance²¹. Yet, a thick and inhomogeneous SEI on Si is still not robust enough to tolerate the large volume change of micro-sized Si, which results in a continuous consumption of the Li and electrolyte, and a loss of active Si (refs. ^{22–24}). Hitherto, no LIB electrolyte was able to reach a cycling CE of >99.9% at a practical loading of large (>10 μm) particle alloying anodes.

Here we report a universal electrolyte design principle for alloy anodes using micro-sized Si, Al and Bi anodes as a demonstration. During lithiation/delithiation, crystal Si experiences reversible changes between amorphous Si and amorphous Li_xSi after the second cycle, and Al and Bi anodes experience changes between crystalline metal and crystalline lithiated alloys. We demonstrate that 2.0 M LiPF₆ in a 1:1 v/v mixture of tetrahydrofuran (THF) and

¹Department of Chemical and Biomolecular Engineering, University of Maryland College Park, College Park, MA, USA. ²Department of Chemistry, Rutgers, The State University of New Jersey, New Brunswick, NJ, USA. ³Department of Chemistry, Rutgers, The State University of New Jersey, Newark, NJ, USA. ⁴Environmental Molecular Sciences Laboratory, Pacific Northwest National Laboratory, Richland, WA, USA. ⁵Center for Functional Nanomaterials, Brookhaven National Laboratory, Upton, NY, USA. ⁶Battery Science Branch, Sensor and Electron Devices Directorate, US Army Combat Capabilities Development Command Army Research Laboratory, Adelphi, MA, USA. ⁷Department of Chemistry and Biochemistry, University of Maryland College Park, College Park, MA, USA. ⁸These authors contributed equally: Ji Chen, Xiulin Fan, Qin Li. ✉e-mail: oleg.a.borodin.civ@mail.mil; cswang@umd.edu

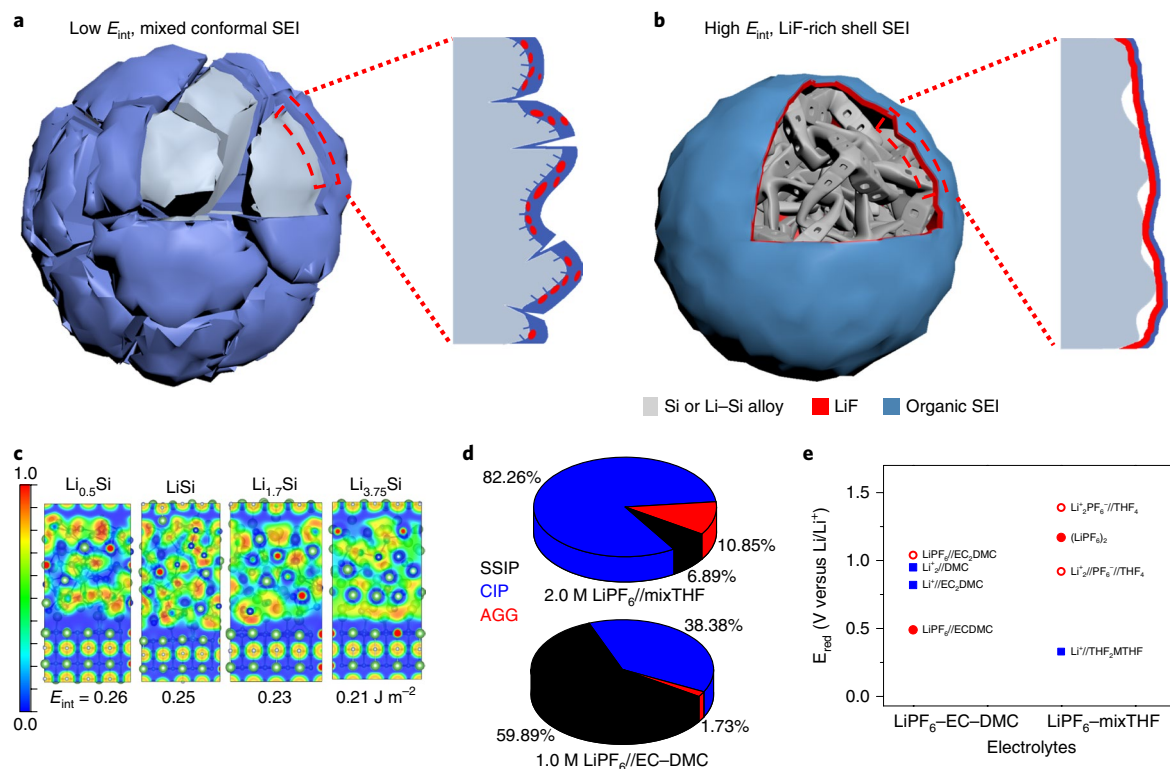


Fig. 1 | Effect of the SEI and electrolyte properties on the alloy anode particles. **a, b**, Schematic of the cycled alloy anode with an organic, low E_{int} and non-uniform (**a**) and an inorganic, high E_{int} and uniform (**b**) Li alloy-SEI interface. **c**, Electron localized function and E_{int} for the Li alloy-LiF interfaces. **d**, Distribution of the Li^+ solvates for the LiPF_6 -mixTHF (2.0 M) and LiPF_6 -EC-DMC (1.0 M) electrolytes from MD simulations. The PF_6^- anions and solvents with $d(\text{Li-P}) < 4.4 \text{ \AA}$ or $d(\text{Li-O}) < 2.8 \text{ \AA}$, respectively, are included in the first Li^+ solvation shell. **e**, Reduction potentials of key electrolyte components with the first Li^+ solvation shell indicated from QC calculations (see Supplementary Figs. 3 and 4 for details). G4MP2, solid symbols; B3LYP/6-31+G(d,p) density functional theory (DFT), open symbols; salt reduction, red symbols; solvent reduction, blue symbols.

2-methyltetrahydrofuran (MTHF) (mixTHF) electrolyte facilitates the formation of thin and uniform lithium fluoride (LiF)-based SEIs with a low adhesion to lithiated alloy surfaces. This enables the SiMPs, AlMPs and BiMPs ($>10 \mu\text{m}$ in size) to provide 2,800, 970 and 380 mAh g^{-1} , respectively, with cycling lives of >200 , a high initial CE of $>90\%$ and a cycling CE of $>99.9\%$ without any pre-treatment, which shows great potential for practical applications of the alloy anodes.

Electrolyte design principle for alloy anodes

Current electrolytes, which include the most successful FEC-containing formulations, form an organic-inorganic SEI that is strongly bonded to the alloy surface, which makes the SEI suffer from the same high deformation as the alloy and leads to breakage and/or reformation of the SEI and alloy pulverization and isolation (Fig. 1a)^{22,23,25,26}. We aim, however, to form a strong SEI with a low adhesion (high interfacial energy (E_{int})) to the alloy surface, so that the alloy can relocate at the interface to accommodate the volume change (Fig. 1b). We first considered the Si anode case. LiF is a suitable SEI candidate as it possesses a high E_{int} with lithium silicate (Li_4SiO_4 , a fully lithiated surface oxide) and Li_xSi (Fig. 1c and Supplementary Fig. 2). When a high-modulus LiF SEI forms on a Si anode, deformation and expansion of Li_4SiO_4 and Li_xSi during cycling occur with little damage to the SEI shell. In addition, the wide bandgap and insulating nature of LiF reduces the thickness of the SEI (increasing the initial CE). Furthermore, the high-modulus LiF shell suppresses the Li_xSi pulverization. The success of the FEC-containing electrolytes for SiMP applications could be rooted in a LiF-contained SEI^{22,23,25,26}. However, the reduction of FEC also

generates organic components in addition to LiF. These organic components increase the adhesion of the SEI to the Li_xSi , which leads to SEI deformation and rupture during the Li_xSi expansion. This SEI design principle is expected to be applicable to a wide range of alloy anodes because of the high interface energy of LiF with their surfaces.

The formation of LiF SEI

The LiPF_6 salt was selected as it reduces to LiF at the anode surface without organic by-products. It is combined with solvents that (1) undergo reduction at low potentials and (2) have a limited solvation ability to Li salts so that the LiF SEI is preferentially formed from LiPF_6 starting at high potentials through the entire lithiation process. The LiPF_6 -reduction potential depends on the extent of ionic aggregation^{27–29}. Owing to the excess electron stabilization on the anion surrounded by multiple Li^+ , electrolytes with a high degree of aggregation are preferred to increase the LiPF_6 -reduction potential²⁸. Thus, our target electrolyte should have a high-degree LiPF_6 salt aggregation and the lowest possible reduction potentials of the solvents to yield a high-purity LiF inner SEI layer. After the formation and/or adjustment of the SEI in the initial cycles, Li_xSi is expected to expand and/or retract within the SEI shell.

For conventional ethylene carbonate–dimethyl carbonate (EC–DMC) (1:1) carbonate electrolytes, solvent-separated ion pairs (SSIPs, black in Fig. 1d) dominated $\sim 60\%$ of the solvation structure, with 38% being contact ion pairs (CIPs, blue) and essentially no ionic aggregates (AGGs, red) (Fig. 1d). The reduction of LiPF_6 CIPs in EC–DMC solvents occurred at potentials close to the those of the reductions of EC and DMC (Fig. 1e). Thus, LiF is expected

Table 1 | Properties of solvents at 25 °C from MD simulations and previous experiments

	THF	MTHF	THF/MTHF
Number of solvents box ⁻¹	512	512	392 (THF), 320 (MTHF)
Equilibration run (ns)	12	13.3	12
Production run (ns)	17.7	12	16.2
Box size (Å)	41.4	44.16	47.72
Density (MD) (kg m ⁻³)	864	850.5	853
Density (experimental) (kg m ⁻³)	882 ^a	849.04 ^b	
Self-diffusion coefficient (MD) (10 ⁻¹⁰ m ² s ⁻¹)	30.8	25.6	29.9 (THF), 28.0 (MTHF)
Self-diffusion coefficient (experimental) (10 ⁻¹⁰ m ² s ⁻¹)	30 ^c		
Viscosity (MD) (mPas)	0.42	0.48	0.45
Viscosity (experimental) (mPas)	0.4631 ^a	0.4776 ^b	
Dielectric constant (MD)	8.1	6.2	6.8
Dielectric constant (experimental)	7.52 ^d	6.97 ^d , 6.4 ^e	

^aDensity and viscosity of THF from Giner et al.⁶². ^bDensity and viscosity of MTHF from Vallés et al.⁶³. ^cSelf-diffusion of THF reported at 303 K from Hayamizu et al.⁶⁴. ^dCRC Handbook of Chemistry and Physics⁶⁵. ^eDelsignore et al.⁶⁶.

to segregate in the organic matrix to form a heterogeneous, mixed organic and inorganic SEI with large separate domains³⁰. Ethers have low thermodynamic reduction potentials (0.0–0.3 V), which makes them good for supporting preferential fluorinated salt decomposition (Fig. 1e and Supplementary Figs. 3 and 4). Among them, salt aggregation increases from linear ethers to mixTHF (Fig. 1d and Supplementary Fig. 5). Importantly, the high degree of LiPF₆ association in the LiPF₆–mixTHF electrolyte (Fig. 1d) pushed the onset of the reduction potential of LiPF₆ above 1.1 V, which is substantially higher than the reduction potentials of mixTHF (Fig. 1e). Thus, a uniform LiF SEI layer is expected to form during the lithiation above 0.1 V and only minor organic components form on the LiF surface near the end of the Si lithiation, in sharp contrast to the mixed organic–inorganic composition of a traditional SEI. The low mixTHF solvent viscosity (Table 1) and poor LiF solvation in mixTHF solvents further enhance the kinetics of the LiF salt aggregation after LiPF₆ reduction. Further validation of the molecular dynamics (MD) predictions was performed via a systematic Raman spectroscopy characterization of the ethers' solvation (Supplementary Note 1).

We further examined the Li⁺ solvation structure, as it controls the salt reduction potential (Fig. 1e). In 1.0 M LiPF₆ solutions, SSIPs decreased from ~60% in carbonate to ~8% in mixTHF (Fig. 1d and Supplementary Fig. 6), whereas CIPs increased from ~38% to 87%, consistent with the drop of the solvent dielectric constant from ~34 for mixed carbonates³¹ to 6.8 for mixTHF (Table 1). A small fraction of the Li⁺PF₆–Li⁺ AGGs (~5%) was observed in the 1.0 M LiPF₆–mixTHF electrolyte, with further increases to 10% as the LiPF₆ salt concentration increased from 1.0 to 2.0 M (Supplementary Fig. 6). A higher salt concentration has three benefits: (1) upshifts the salt decomposition potential to above 1.17 V (Fig. 1e and Supplementary Fig. 7b), which facilitates LiF formation due to a higher aggregation, (2) earlier-formed LiF SEI suppresses the solvent reduction to lower potentials, which inhibits the formation of organic components in the SEI during alloy expansion and (3) extends the electrolyte oxidation potential to >4.2 V (Supplementary Note 2) for the 2.0 M LiPF₆–mixTHF electrolyte (the designed electrolyte) (Supplementary Figs. 7a and 8a) as the fraction of free solvent decreases. Further extension of the ether-based electrolyte anodic stability is possible^{32,33}. In the designed electrolyte, the dominant LiPF₆ reduction forms an initial LiF SEI and repairs the broken LiF SEI by newly

formed pure LiF during lithiation because mixTHF solvents do not reduce until at the end of lithiation. Only at very low voltages does the solvent start to decompose to provide a thin layer of organic shell outside the LiF layer because the very low electronic conductivity of LiF also limits the reduction of mixTHF solvents. Such a homogeneous LiF–organic bilayer SEI, formed after the full alloy lithiation, is expected to be thin and hold the lithiated alloy together. It allows the lithiated alloy underneath LiF to deform elastically and plastically due to the high E_{int} at the LiF–alloy interface, and thus maintains the integrity of alloy microparticles during expansion and/or shrinkage (Fig. 1b). Therefore, the LiF–organic SEI bilayer functions as a robust shell that strongly holds the ruptured or flowed alloy together rather than isolating the ruptured alloy due to the organic-dominated SEI formed in traditional electrolytes (Fig. 1a).

Electrochemical performance of SiMPs

A Si electrode with a ~2.0 mg cm⁻² loading exhibited a high capacity of 5.6 mAh cm⁻² and ~2,800 mAh g⁻¹ at a current density of C/5 (1C = 3,579 mA g⁻¹ (Fig. 2a)) in the designed electrolyte. The high cycling stability is demonstrated by the overlapped charge/discharge curves after the second cycle (Fig. 2a). The capacity retention after 400 cycles was 90.0% (Supplementary Fig. 9). The high and stable capacity indicates that SiMPs are well utilized and remain electronically connected during repeated electrochemical lithiation/delithiation. The initial CE was 90.6% and the CE reached >99.9% at the seventh cycle and maintained thereafter (Fig. 2e and Supplementary Fig. 9), which is higher than the CE of small SiMPs (1–3 μm) confined by a graphene cage²¹ or using an elastic binder¹⁸. In 1.0 M LiPF₆–EC–DMC (a traditional electrolyte), ~40% of the capacity was lost within 20 cycles (Fig. 2b) and only ~8% was maintained after 50 cycles. The CEs were 96–97% in the first several cycles and only hovered around 98.0% after the 50th cycle with a low specific capacity of 200 mAh g⁻¹. Increasing the salt concentration to 2.0 M in LiPF₆–EC–DMC electrolyte did not improve the cycling stability (Supplementary Fig. 10) and even decreased the specific capacity due to the increased electrolyte viscosity.

The rate capability of the SiMPs in the designed electrolyte also far exceeds that in the traditional electrolyte. As shown in Fig. 2c,d, at a discharge rate of 1C (3.58 A g⁻¹), the Si electrode can retain over 2,400 mAh g⁻¹, whereas only 1,098 mAh g⁻¹ was achieved in the traditional electrolyte (Supplementary Fig. 11). Even at 3C, a capacity

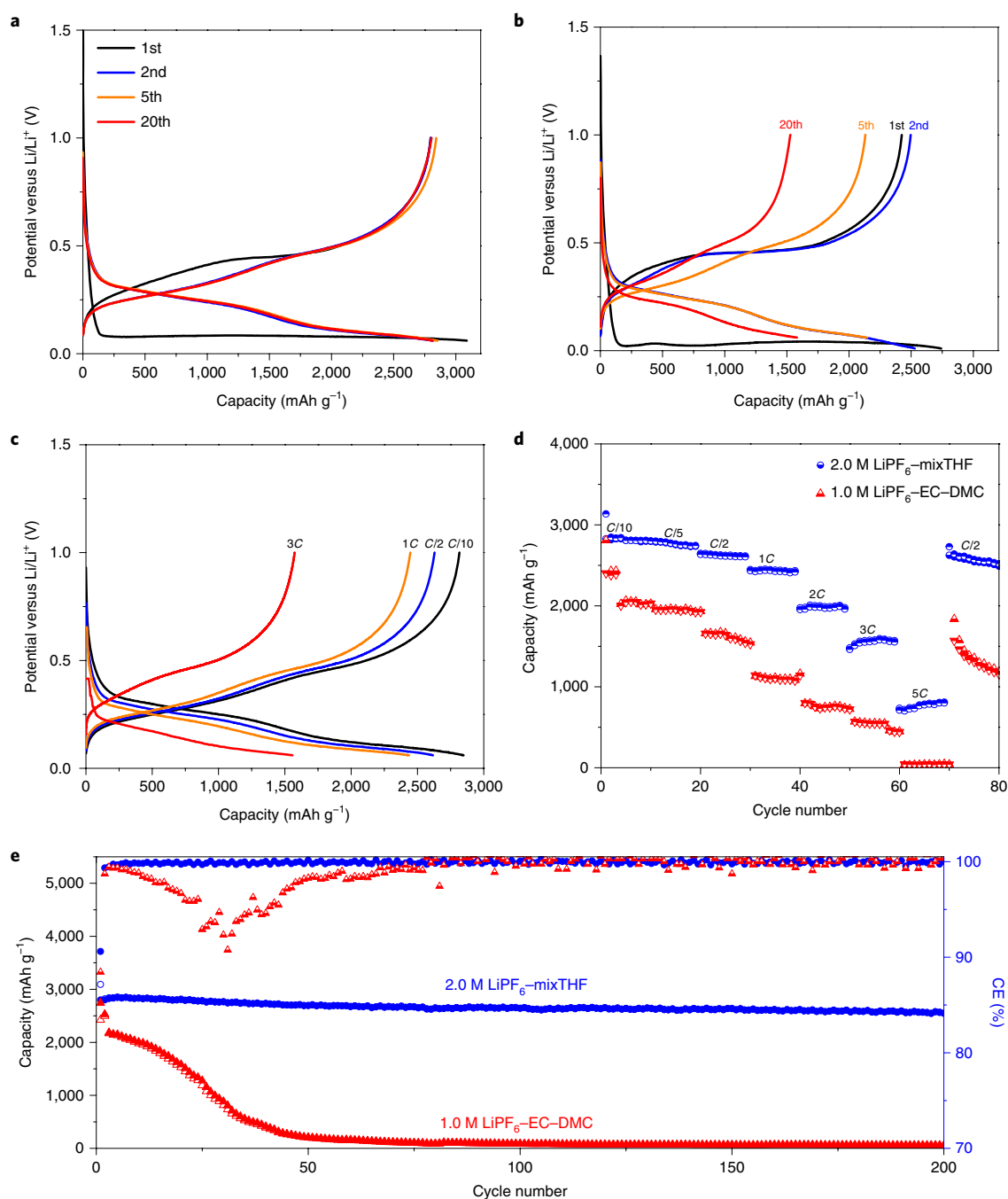


Fig. 2 | Cycling performance of SiMP electrodes in half-cells. a–d, Typical charge/discharge profiles of a SiMP electrode cycled in different electrolytes, 2.0 M LiPF₆-mixTHF (**a**), 1.0 M LiPF₆-EC-DMC (**b**). **c**, Charge/discharge curves at different rates of Si cycled in 2.0 M LiPF₆-mixTHF. **d**, Rate performance comparison. **e**, Cycling stability and CEs of SiMPs cycled in 2.0 M LiPF₆-mixTHF and 1.0 M LiPF₆-EC-DMC electrolytes; the rate is C/5.

of 1,580 mAh g⁻¹ was still reached in the designed electrolyte. The excellent rate performance was also verified on a pure Si film (Supplementary Note 3). Importantly, SiMPs also showed an outstanding low-temperature performance in the designed electrolyte (Supplementary Fig. 12). As the temperature dropped to -20 and -40 °C, reversible capacities of 2,304 and 1,475 mAh g⁻¹, respectively, were achieved, whereas only 658 and 0 mAh g⁻¹ were reached in the traditional electrolyte. The cycling, rate and low-temperature performances are attributed to the thin and stable SEI, as evidenced by the small and almost-constant SEI resistance during cycling shown by impedance spectra collected at the fully lithiated state

(Supplementary Fig. 13a). On the contrary, the SEI resistance in the traditional electrolyte first decreases from the first to the fifth cycle as SiMP fractures and increases the surface area³⁴ (Supplementary Fig. 13b), followed by an impedance increase due to the continuous growth and thickening of the SEI on the electrode, consistent with previous reports³⁵.

Performances of AIMP and BiMP anodes

The AIMP showed a flat lithiation/delithiation plateau centred at 0.4 V (a phase transition process (Fig. 3)). The thermodynamic potential hysteresis was only about 0.04 V in the phase transition

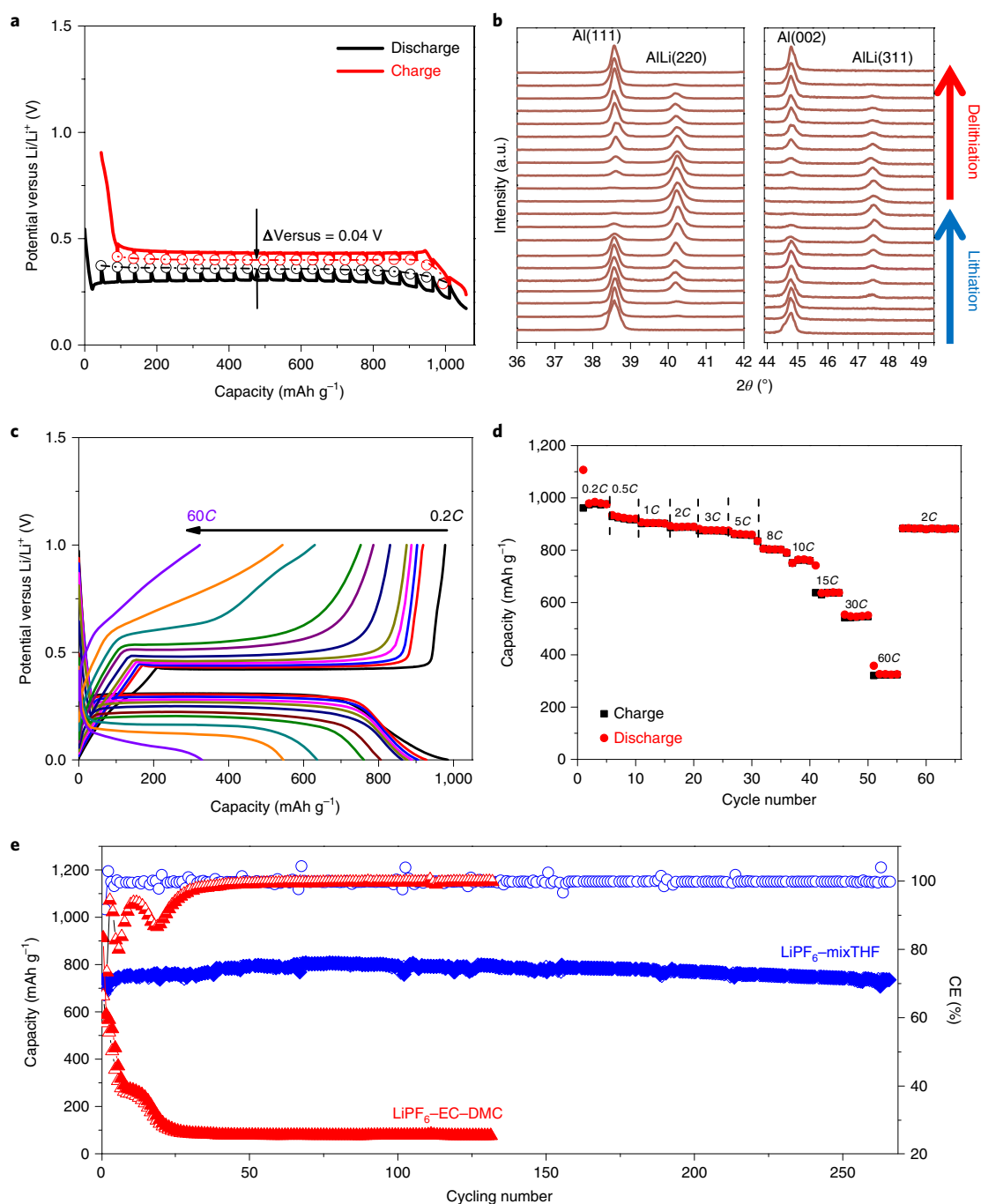


Fig. 3 | Electrochemical performance of AIMP electrodes in half-cells. **a**, Galvanostatic intermittent titration technique profiles of the AIMP electrode in the designed 2.0 M LiPF_6 -mixTHF electrolyte. **b**, XRD results of the AIMP electrode during the lithiation/delithiation process. The XRD data were collected in the third charge/discharge cycle. **c,d**, Charge/discharge curves (**c**) and rate performance (**d**) of AIMP cycled in the designed electrolyte. **e**, Cycling stability and CEs of AIMPs cycled in the designed and traditional 1.0 M LiPF_6 -EC-DMC electrolytes. a.u., arbitrary units.

region. X-ray diffraction (XRD) (Fig. 3b) shows that the crystalline Al and LiAl phase transitions take place in the charge/discharge process, in line with the ideal flat charge/discharge profiles. The absence of Al or LiAl peaks in the fully lithiated or delithiated states, respectively, indicates the full conversion of all the active material in the charge/discharge cycles.

The AIMP electrode demonstrated a good rate capability in the designed electrolyte (Fig. 3c,d). At 30C, a more than 50% capacity was achieved, and when returned to 2C, a capacity of $\sim 900 \text{ mAh g}^{-1}$ was recovered, which indicates tolerance of the rapid

phase transitions. Figure 3e compares the long cycling performances in the designed and traditional electrolytes. The capacity decayed to less than 10% of its initial capacity with a cycling CE of only $\sim 85\%$ in the first 20 cycles in the traditional electrolyte, consistent with previous reports³⁶. In sharp contrast, no capacity decay was observed in the designed electrolyte for over 260 cycles. The CE reached 91.6% in the initial cycle and jumped to $>99.9\%$ at the eighth cycle and remained $>99.9\%$ thereafter, which is much higher than the CE of nano-Al confined by a titanium oxide cage¹⁰, and even comparable to the commercial mesocarbon microbead anodes³⁷. The stability

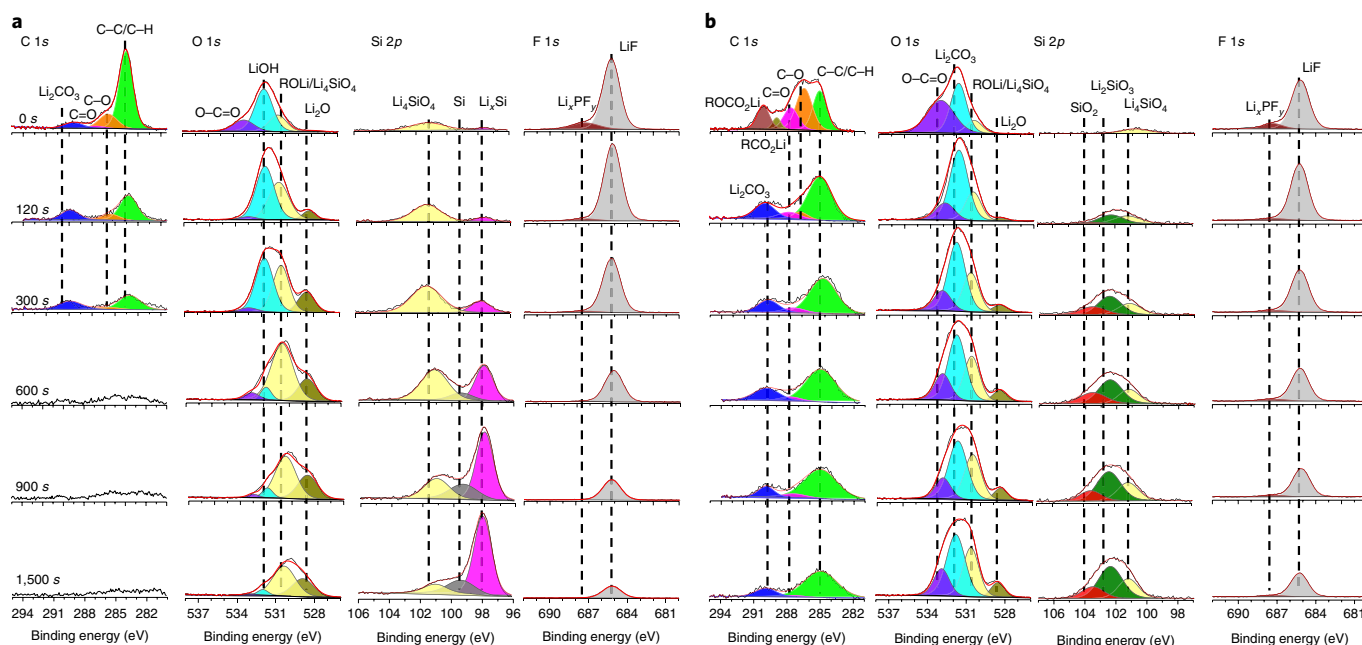


Fig. 4 | SEI chemical composition. **a, b**, XPS characterization of the SEI formed on Si cycled using electrolytes 2.0 M LiPF₆-mixTHF (**a**) and 1.0 M LiPF₆-EC-DMC (**b**). The C 1s, O 1s, Si 2p and F 1s spectra are displayed in columns, which show the corresponding depth profiling results.

difference is attributed to the repeated breakage and growth of the SEI in the traditional electrolyte, as indicated by the increased hysteresis (Supplementary Fig. 14).

The electrolyte also supports the BiMP electrode (Supplementary Figs. 15 and 16). No capacity decay was observed for over 250 cycles at 2C with a high cycling CE of >99.9%. At a 60C rate, a 50% capacity was retained.

Characterization of the SEI on the cycled Si thin film

The SEI chemical composition was examined via X-ray photoelectron spectroscopy (XPS) with an Ar⁺ sputtering depth profiling (Fig. 4a). The top surface of the SEI consisted of both organic (RCH₂OLi) and inorganic (Li₂O, LiF) components. XPS elemental analysis after different Ar⁺ sputtering times shows that the content of carbon, indicative of organic decomposition products, decreases with increasing sputtering time to less than 10% after 120 s (Supplementary Fig. 17). Specifically, in the Si spectra, Li₄SiO₄, Si and Li-Si alloy dominate, with the Li-Si alloy signal reaching about ~50% of all the Si signals at 600 s of sputtering, which is assumed as the SEI-Si interface. The C 1s signal drops to the noise level before reaching the SEI-Si interface, accompanied by a decrease in the carbon-related O-C=O signal in the O 1s spectra. Meanwhile, the LiF signal is still strong at the SEI-Si interface and persists throughout the whole sputtering process, consistent with the proposed LiF-organic bilayer SEI structure in Fig. 1b, although minor LiF products also exist in the organic overlayer of the SEI. The existence of crystalline LiF in SEI was also verified by the electron diffraction patterns obtained during cryogenic transmission electron microscopy (cryo-TEM) experiments (Supplementary Fig. 18). In addition, the signals of Li₄SiO₄ in both the O 1s and Si 2p spectra reach their maximum at the SEI-Si interface. The absence of a SiO_x peak for Si cycled in the designed electrolyte further confirms a complete and homogeneous lithiation of the SiO_x layer due to a uniform SEI. This elastic Li₄SiO₄ layer on the Li-Si alloy is also beneficial to the integrity of the Si electrode³⁸. The elemental composition of the bilayer SEI was confirmed by cryo-TEM with energy dispersive X-ray (EDX) line scans (Supplementary Note 4).

The surface of the SEI formed in the traditional electrolyte (Fig. 4b) consists of both organic RCH₂OCO₂Li and LiF. The carbon and LiF signals persist, but no Si and Li_xSi peaks appear during the sputtering, which indicates the SEI is made up of mixed organic-LiF compounds from the surface to the inner part, and the SEI layer is much thicker compared with that generated in the designed electrolyte. The LiF signal intensities in the traditional electrolyte are lower compared with those from the SEI in the designed electrolyte, which indicates less LiF is generated in the traditional electrolyte. This is because the carbonates are reduced at a higher potential and contribute more to the SEI compared with the ethers³⁹. In addition, the O 1s spectra of the SEI formed in the traditional electrolyte also exhibit less Li₂O content, which indicates insufficient lithiation of the SiO_x on SiMPs. Moreover, in the Si 2p spectra, the original SiO_x peak emerges after sputtering for 300 s in the case of the carbonate electrolyte, but not in the designed electrolyte. This remaining SiO_x indicates incomplete lithiation of the surface oxide, and leads to a higher inhomogeneity and resistance to Li⁺ diffusion and slow kinetics. The non-uniform lithiation due to a non-uniform organic-inorganic SEI also induces a high stress and strain at places where expansion is highly inhomogeneous, which easily breaks the weak, mixed organic-inorganic SEI. Consequently, repeated breaking and/or reforming of the SEI leads to a low CE and poor stability.

Distribution of LiF in the SEI was acquired by electron energy loss spectroscopy (EELS) spectral imaging. Li compounds commonly found in the SEI have a rather different valence plasmon energy and peak width⁴⁰. Hence, plasmon signals were used to successfully differentiate them, and severe damage by the electron beam can be avoided at room temperature⁴¹. Using this approach, we performed spectral imaging in the plasmon energy range for cycled Si particles and analysed the composition at each pixel. A hollow region in the middle of each spectral image was caused by electron mean-free-path limitations, and trace Li was transformed from the LiF on beam irradiation. For Si cycled in the designed electrolyte, we found a thin surface layer of LiF (Fig. 5a,b), which supports the proposed mechanism (Fig. 1b). The composition near the surfaces varies within a small depth (spectra in Fig. 5c). A relatively

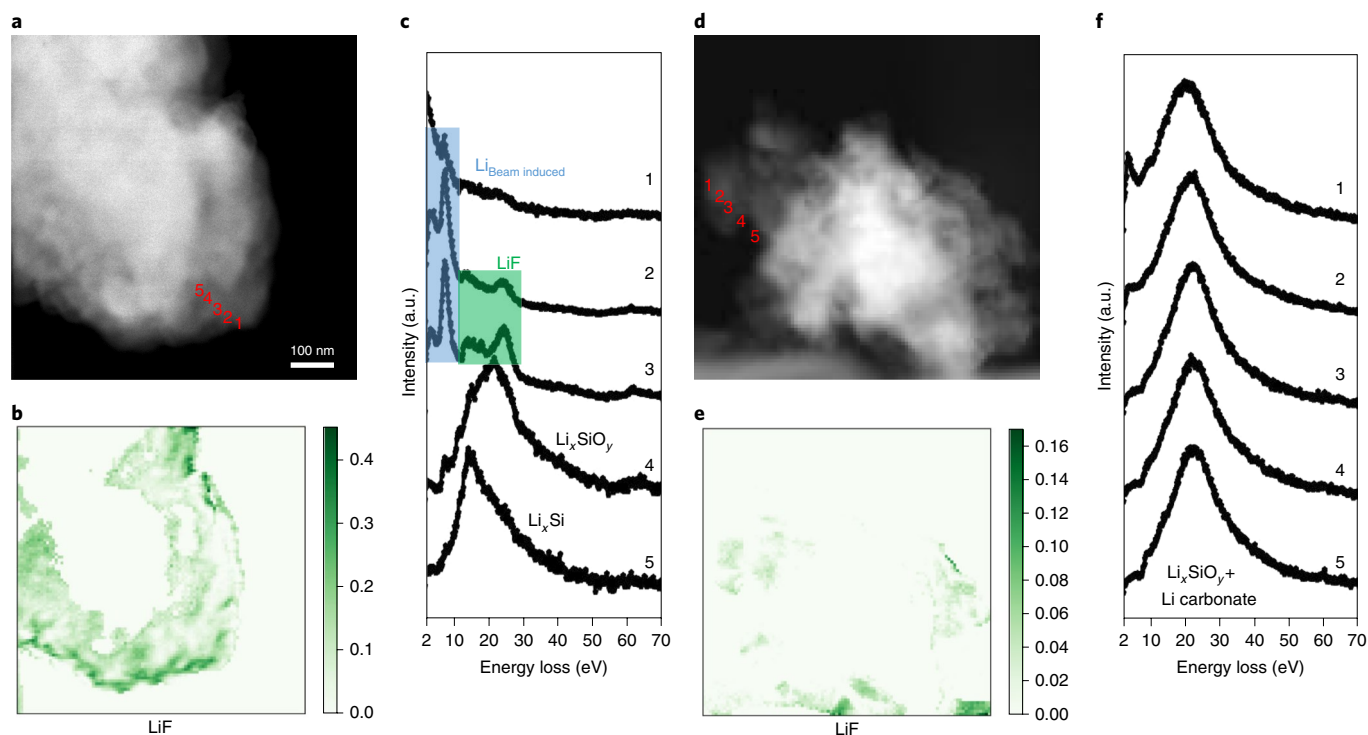


Fig. 5 | LiF distribution on Si. **a,d**, High-angle annular dark-field imaging images. **b,c,e,f**, EELS spectral images showing the LiF distribution and percentage of the scanned area (**b,e**), as well as five (labelled 1–5 from surface to the inner layers) typical EEL spectra near the surfaces of the Si particles (**c,f**). The electrolytes are 2.0 M LiPF₆-mixTHF (**a–c**) and 1.0 M LiPF₆-EC-DMC (**d–f**).

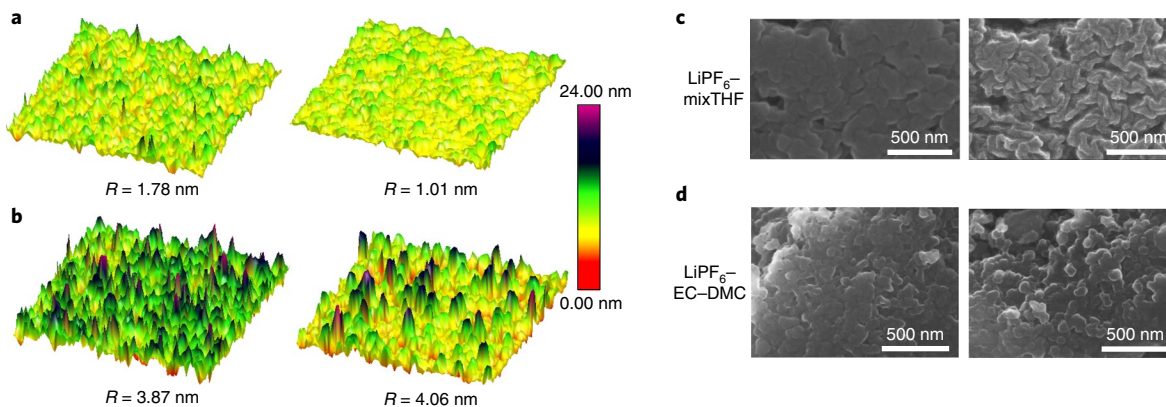


Fig. 6 | Morphology of Si anodes after cycling. **a,b**, Typical electrochemical AFM surface roughness (R) comparison at the lithiated (left) and delithiated (right) states, area $2 \times 2 \mu\text{m}$. **c,d**, SEM images of the SiMP electrode after 100 cycles of operation in different electrolytes before (left) and after (right) electron-beam irradiation. The electrolytes are 2.0 M LiPF₆-mixTHF (**a,c**) and 1.0 M LiPF₆-EC-DMC (**b,d**).

sharp valence plasmon peak from LiF at $\sim 25 \text{ eV}$ is clearly visible on the outer layer. Underneath the LiF layer, a Li_xSiO_y sublayer (Supplementary Fig. 19a) and Li_xSi are observed, which indicates the LiF– Li_xSiO_y – Li_xSi structure. For Si cycled in traditional electrolytes, a mixed organic–inorganic SEI (Fig. 5d) with a broad peak centred around 22 eV is found for almost all of the near-surface spectra (Fig. 5f), which indicates that there is no substantial amount of LiF on the surfaces (Fig. 5e).

The roughness and thickness of the SEI during dynamic lithiation/delithiation was studied by in situ electrochemical atomic force microscopy (AFM). A super-smooth Si wafer ($\sim 0.18 \text{ nm}$ roughness; Supplementary Fig. 20) was used to monitor the surface morphological evolution. In the designed electrolyte, the roughness increased

to $\sim 1.78 \text{ nm}$ at the lithiated state and reduced to $\sim 1.01 \text{ nm}$ after delithiation (Fig. 6a), much smaller than the values from the traditional electrolyte, 3.87 and 4.06 nm (Fig. 6b). The different roughness is consistent with the XPS Si $2p$ spectra, which shows that SiO_x is uniformly fully lithiated in the designed electrolyte and non-uniformly partially lithiated in the traditional electrolyte. The fourfold greater roughness in the traditional electrolyte indicates a $\sim 400\%$ strain applied to the SEI layer by lithiated Si compared with that of the designed electrolyte. In addition, the decreased roughness during delithiation in the designed electrolyte reflects that the LiF–organic bilayer SEI suppresses the irregular volume expansion and holds the Si together, which cannot be achieved by the mixed organic–inorganic SEI from the traditional electrolyte (roughness increases after

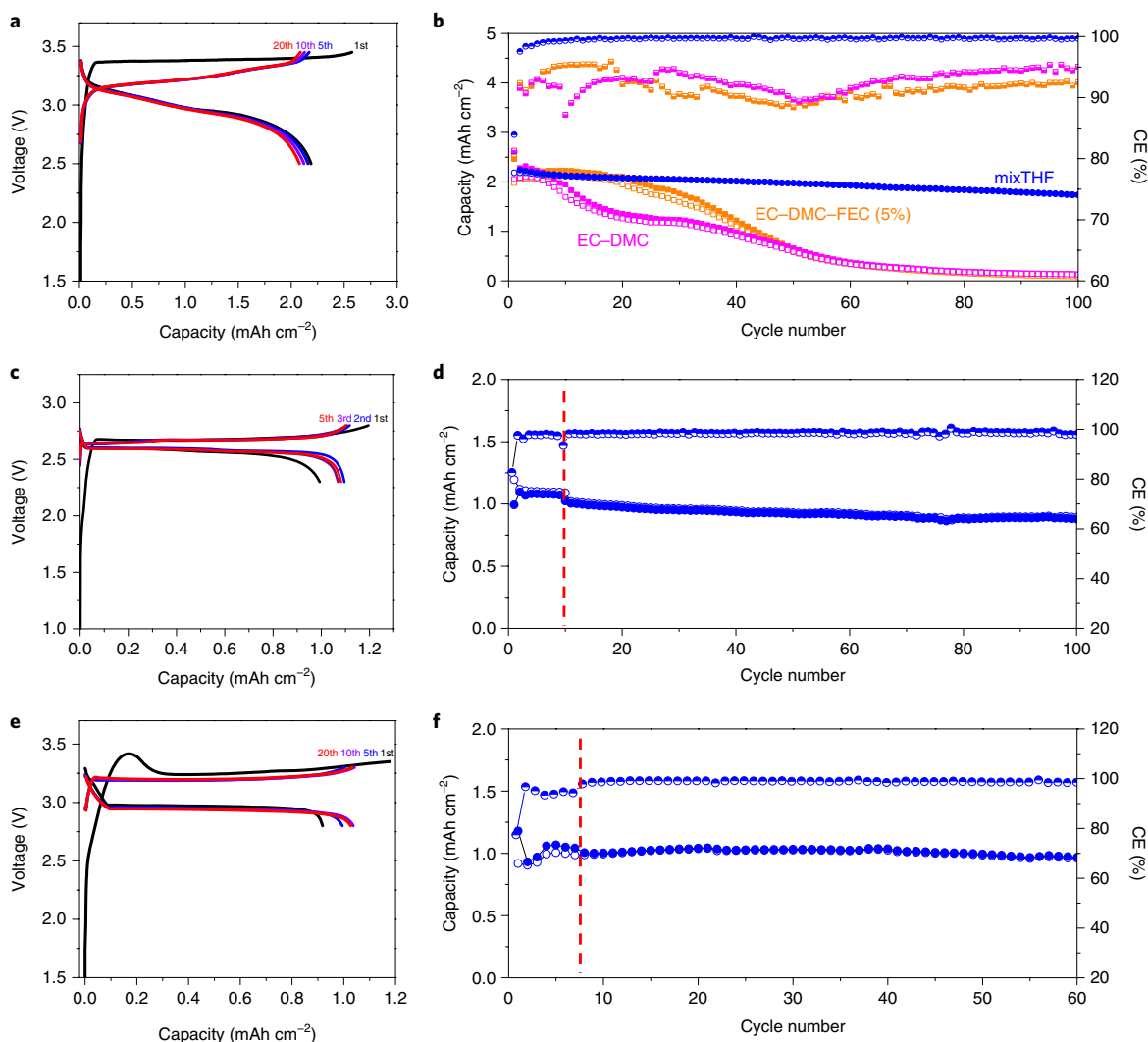


Fig. 7 | Cycling of the SiMP, BiMP and AIMP/LFP full cells. **a–f**, Typical charge–discharge profiles of the SiMP, AIMP and BiMP/LFP full cells (**a,c,e**, respectively) and full-cell cycling performance along with the CEs (**b,d,f**, respectively). The red dashed lines indicate the rate change and the blue symbols denote cycling using the 2.0 M LiPF₆-mixTHF electrolyte.

delithiation). The thicknesses of the SEI bilayers are 0.37 nm for LiF and 2.5 nm for the organic layer (Supplementary Note 5).

The high E_{int} between the LiF SEI and lithiated Si and Li_xSiO₄ (Fig. 1c and Supplementary Fig. 2) allows lithiated Si to expand and shrink to form a core–shell structure in the designed electrolyte (Fig. 1b), which was confirmed by scanning electron microscopy (SEM) (Fig. 6c and Supplementary Figs. 21–23). As the SEI is sensitive to the electron beam, selected-area electron-beam irradiation was applied to gradually remove the SEI. After removing the SEI for different times, the underneath walnut-like Si (or Li_xSi) gradually becomes visible (Supplementary Fig. 21). It is obvious that the bulk SiMPs with a polyhedral shape and rough surfaces (Supplementary Fig. 22a) evolved into a walnut-like integrity (Supplementary Figs. 22c and 23) coated with a smooth LiF–organic bilayer SEI (Fig. 6c and Supplementary Fig. 22b,d, barely irradiated area) after cycling in the designed electrolyte. This is the result of a repeated plastic flow of the relatively soft Li_xSi within the stiff LiF-rich SEI, which holds the Si together and limits rupturing (Supplementary Note 6). Any new cracks within the SEI during lithiation can be quickly healed by new LiF, which leads to the development of the walnut-like Si integrity protected under the SEI after cycling without any pulverization. Such a lamellar-like morphology of Si allows expansion in the direction

perpendicular to the lamellar and the creation of the relatively small new LiF SEI surface needed to accommodate Li_xSi growth during lithiation. Moreover, a stiff LiF SEI is likely to withstand stress and prevent a void collapse during delithiation, which makes these voids available to accommodate Li_xSi expansion during the next cycle. In addition to the favourable mechanical properties, the LiF SEI layer is known to possess a high ionic-to-electronic conductivity ratio⁴², and thus a thin layer is sufficient to inhibit the unwanted electrochemical reactions. On the contrary, the organic components in the organic–inorganic SEI formed in the traditional electrolyte have a low E_{int} with the Li_xSi and thus strongly bond to the Li_xSi surface and experience a similar degree of deformation as the lithiated Si during the volume changes, as demonstrated by the similar pulverized particle morphology before and after electron-beam irradiation (Fig. 6d). In addition, the shear modulus of the organic-rich SEI is an order of magnitude lower than that of LiF (ref. 43), which is unable to withstand the large elastic stress before the plastic deformation and results in the pulverization of Si.

Full-cell performance

The designed electrolyte also enables LiFePO₄ (LFP, with a 2.3 mAh cm^{−2} loading) and NCA (with a 1.6 mAh cm^{−2} loading)

cathodes to achieve good cycling stability (Supplementary Figs. 24, 25). We constructed practical SiMP-, AlMP- and BiMP//LFP and SiMP-, AlMP- and BiMP//NCA full cells (Fig. 7 and Supplementary Fig. 26). Neither precycling of the anodes or cathodes, nor prelithiation of these SiMP, AlMP or BiMP anodes was performed. All of these full cells exhibit a stable cycling and a high CE (which approaches 100% after the fifth cycle) at practical values of current density and areal capacity. Moreover, no increases in the overpotentials were observed in the voltage profiles for all of these full cells at various cycle numbers, which indicates that both the electrodes and their electrode-electrolyte interfaces remain stable during cycling. Preliminary SiMP//NCA full cells retained 92% capacity after 30 cycles (Supplementary Fig. 26). The SiMP//LFP full cell retained 80% capacity after 100 cycles in the designed electrolyte, whereas only 4.5% and 6.2% remained in the traditional electrolyte and with the FEC additive, respectively (Fig. 7b). The severe capacity decay is due to the continuous SEI growth on the SiMP anode, which leads to both a low CE and increasing hysteresis (Supplementary Fig. 27).

Conclusions

The SEI inner layer that contacts with alloy material should be purely inorganic with a high interface energy with the lithiated alloy and a high mechanical strength to accommodate the large volume change of the alloy anodes. A rationally designed 2.0 M LiPF₆-mixTHF electrolyte enabled us to selectively form such a LiF-organic bilayer SEI on micro-sized alloying anodes, which allows SiMPs, AlMPs, and BiMPs to undergo elastic and plastic deformation within the SEI shell. SiMPs in the electrolyte provided a high capacity of 2,800 mAh g⁻¹ and 5.6 mAh cm⁻² for over 400 cycles with an initial CE of 91% and a cycling CE of >99.9%. The SiMP//LFP full cell exhibited a >100 cycles life with a high cycling CE that approaches 100% at a practical capacity of >2.0 mAh cm⁻². The initial cycling of the AlMP//LFP, BiMP//LFP and SiMP//NCA full cells also demonstrated a stable and promising performance. Thus, our finding suggests a simple drop-in electrolyte modification, which leads to high-energy, micro-sized alloying anode-containing batteries operating at a practical areal capacity and charge-discharge rates.

Methods

Preparation of electrodes and electrochemical measurements. For the SiMP electrodes, a slurry was first prepared by dispersing SiMPs (–325 mesh, as-received, >10 µm in size, as revealed by SEM in Supplementary Fig. 28 and crystalline, as confirmed by XRD), lithium polyacrylate binder (10 wt% aqueous solution) and Ketjen black in water with a weight ratio of 6:2:2. For the AlMP and BiMP electrodes (Supplementary Figs. 29 and 30), the weight ratio is changed to 8:1:1. The slurry was cast onto a copper (Cu) foil, dried at room temperature for 24 h and further dried at 90 °C overnight under vacuum. The Si electrode (with multilayer SiMPs; Supplementary Fig. 31) processing is the same as that of commercial graphite electrodes without any additional pretreatment or prelithiation. CR2032 coin-type half-cells were assembled by sandwiching one piece of polyethylene separator (Celgard) and one piece of glass fibre between the SiMP electrodes and Li metal foil. The electrolytes used for cell assembly were: (1) 1.0 M LiPF₆ in 1:1 (v/v) EC-DMC, (2) 1.0 or 2.0 M LiPF₆ in 1:1 (v/v) THF-MTHF, (3) 1.0 M LiPF₆ in triglyme (G3) and (4) 1.0 M LiTFSI (TFSI, bis(trifluoromethanesulfonyl)imide) in 1:1 (v/v) mixTHF. For the AlMP and BiMP electrodes, a similar protocol was applied for the electrode preparation.

In the galvanostatic cell tests, the current density was set at 0.2 C (1 C = theoretical capacity) in the potential range 0.06–1.0 V versus Li/Li⁺ using a battery cycler (Landt). For electrolytes other than LiPF₆-mixTHF, two activation cycles with a voltage cutoff of 0.005 V were performed before the cycling test. Both the specific capacities and current densities are based on the SiMP mass only.

For SEM imaging of the electrodes after cycling, the electrodes were washed with MTHF to remove any residual Li salts from the surface of the electrodes. For full-cell testing, LFP and NCA cathodes coated on Al foil were kindly provided by Saft America Inc. The cells were charged with a cutoff voltage of 2.5–3.45 V (LFP) or 2.7–4.1 V (NCA). For the full-cell configuration, to compensate the Li consumption due to the SEI and cathode electrolyte interphase formation in the first several cycles, the capacity ratio of the cathode and anode was set as 1.3.

For XPS tests, we sputtered Si on a Cu foil as a working electrode to exclude the elemental interference of conductive carbon and binder, which enabled monitoring of the thickness depth-dependent SEI information. Experimentally, the Li/

half-cells were disassembled in the delithiated state after 50 lithiation-delithiation cycles to examine the SEI on the Si surface. Samples were transferred into the XPS chamber under argon (Ar) protection to avoid any contamination by air.

Scanning transmission electron microscopy–EDX spectroscopy. The composition of the SEI was also explored via scanning transmission electron microscopy (STEM)–EDX line scans with a Hitachi HD2700C dedicated STEM with a probe corrector operated at 200 kV. To minimize the damage of the SEI from the electron beam, a liquid nitrogen cryotransfer holder was employed. In addition, TEM sample preparation and loading were performed in an Ar-filled glove box for the whole procedure to avoid exposure to air and moisture⁴⁴.

STEM EELS. EELS was performed using the Nion UltraSTEM 100 STEM at Rutgers University. Electrons were accelerated at 60 kV with a beam current of ~4 pA. Both convergence and EELS collection angles were set to 30 mrad. Spectral images were taken from 800 × 800 nm areas using 100 × 100 pixels. EEL spectra were collected with a dispersion of 0.15 eV per channel and a 20 ms dwell time. No changes were observed from annular dark-field images after the spectral imaging. The TEM samples used were also prepared in an Ar-filled glove box. To analyse the composition at each pixel, single scatterings from 3 to 50 eV were extracted from each EEL spectra by Fourier log deconvolution. The percentage of each compound was then determined by multiple linear regression. Fitting was not attempted for thick areas (thickness/λ > 2.5, where λ is the inelastic mean free path of 60 kV electrons in the material), which leaves a hollow region in the middle of each spectral image. A thin layer of Li metal was detected on the perimeter of LiF-covered Si. We found this is because the near-surface, thinner region of LiF is more prone to electron-beam damage than the bulk, thicker part. Also, Li metal was transformed from LiF by electron-beam radiation. This observation was confirmed by performing similar EELS mapping on reference LiF crystals.

AFM. The in situ electrochemical AFM was conducted with a Dimension ICON atomic force microscope set up inside an Ar-filled glove box, in which both the H₂O and O₂ levels were below 0.1 ppm, coupled with a CH Instrument 760E potentiostat. For all the topographical mappings, a ScanAsyst-Fluid+ probe (Bruker AFM Probes) was used with a nominal spring constant of 0.7 N m⁻¹, composed of a silicon nitride cantilever with a sharp Si tip. This probe was also used to remove the soft SEI layer. An RTESPA-525 probe (Bruker AFM Probes) with a nominal spring constant of 200 N m⁻¹ was used to remove the hard SEI layer from the substrate, which is composed of antimony-doped Si with a Si tip. The cycling was conducted against a Li metal foil in an electrochemical cell designed for LiB materials and sealed during the AFM operation.

To measure the thickness of the soft SEI layer, first the contact mode was operated with a ScanAsyst-Fluid+ probe with a contact force of 20 nN to remove the soft SEI layer in a 1.5 × 1.5 cm² scanning area. Higher contact forces were also applied to assure that there was no softer SEI layer to be removed. Afterward, the same probe was used to conduct the peak-force tapping mode to image the morphology in a 5 × 5 cm² area, which included the brushed region. This topography mapping compares the height between the brushed and unbrushed regions to measure the thickness of the soft SEI layer.

To measure the hard SEI thickness, an RTESPA-525 probe was used with a contact force of 3.0 µN to remove all the SEI layers from the Si substrate. Higher forces were also applied to make sure that no SEI layer was left on the substrate. (As the Young's modulus of Si is over 100 GPa, this probe was chosen because it can only penetrate through surfaces with a maximum of 20–30 GPa.)

AFM sample preparation. The substrate used for the electrochemical AFM measurements was a polished boron-doped Si (University Wafer) with a resistivity of 0.001–0.005 Ω cm. The substrate was cut to an almost 1 cm² surface area, and the surface area was then accurately measured for a charge/discharge applied current of 20 µA cm⁻². Then it was rinsed with water and submerged into a freshly made Piranha solution (H₂SO₄:H₂O₂, 3:1) for 3–5 min. After that, the substrate was thoroughly rinsed with an excessive amount of ultrapure deionized water (18.2 MΩ cm) and was dried with 99.998% nitrogen gas. The backside of the substrate was scratched to obtain the pure Si (more conductive) part and then was conductively glued to a thin Cu foil as a conductor using Pelco conductive carbon glue. The borders of the substrate were then glued to a Teflon adaptor using Torr Seal Sealant (Varian Vacuum Technologies) and were left for more than 24 h for both the conductive glue and the sealant to cure. The substrate was then assembled into the Bruker electrochemical cell and kept under vacuum overnight before inserting it into the glove box for the electrochemical AFM measurements.

Calculation on the a-Li₂Si–LiF interface energy. First-principles calculations based on DFT were performed to study the a-Li₂Si–LiF interface using the Vienna Ab Initio Simulation Package with the Projector Augmented Wave method^{45–48}. The exchange-correlation energy was described by the functional of Perdew, Burke and Ernzerhof^{49,50}. The energy cutoff of the electron wavefunction was set to be 520 eV. The geometry optimizations were performed using the conjugated gradient method, and the convergence threshold was set to 10⁻⁵ eV in energy and 0.01 eV Å⁻¹ in force. The work of separation for the a-Li₂Si–LiF interface is defined by

Table 2 | Electrolyte properties from MD simulations

	LiPF ₆ -EC-DMC	LiPF ₆ -G3	LiTFSI-mixTHF	LiPF ₆ -mixTHF	LiPF ₆ -mixTHF
Number of solvents box ⁻¹	480 (EC), 352 (DMC)	354	392 (THF), 320 (MTHF)	392 (THF), 320 (MTHF)	392 (THF), 320 (MTHF)
Number of salts box ⁻¹	64	64	64	64	128
Molarity <i>c</i> (mol l ⁻¹)	1.0	0.95	0.88	0.95	1.88
Rounded molarity (M)	1	1	1	1	2
Equilibration run (ns)	39	34.8	65	39.2	25
Production run (ns)	67.6	19	20	30.0	39
Box size (Å)	47.49	48.18	49.46	48.24	48.9
Ionic conductivity (mS cm ⁻¹)	13.2	1.3	5.4	4.3	4.0
SSIP (%)	60	47	28	7.9	6
CIP (%)	38	52	71	86.7	83
AGG (%)	2	1	1	5.5	10

The simulation set-up is listed at the top and the properties calculated from simulations at 25 °C at the bottom. As, in principle, the Li-ion solvation structure consists of SSIPs, CIPs and AGGs, we also list the percentage of these components in each electrolyte. SSIPs, CIPs and AGGs have a distinct number of Li⁺ coordinating anions—when defining the solvation structure within a 4.4 Å radius of phosphorus in PF₆⁻ or nitrogen in TFSI⁻, the coordination numbers are 0, 1 and 2, respectively.

$W_{\text{sep}} = (E_{\text{a-Li}_x\text{Si}} + E_{\text{LiF}} - E_{\text{a-Li}_x\text{Si-LiF}})A$, where $E_{\text{a-Li}_x\text{Si}}$, E_{LiF} and $E_{\text{a-Li}_x\text{Si-LiF}}$ are the total energy of the a-Li_xSi slab, LiF slab and a-Li_xSi-LiF interface and A represents the total interface area. To model the slabs, a vacuum layer larger than 12 Å was applied for Li₃SiO₄-LiF interface. In the electron-localized function, red represents covalent, yellow ionic and green metallic bonding (Fig. 1c, Supplementary Fig. 2).

In the bulk, the covalent Si-Si bonds are replaced with ionic Li-Si bonds with increasing Li concentration to form a weak bond of mixed ionic-covalent character, with a substantial charge depletion of the Li atoms and a charge accumulation of the Si atoms. The formation of weaker Li-Si bonds is expected to result in a transition from brittle to ductile with increasing Li concentration, consistent with the experimental results. The interface bonding is also mainly contributed by weak metallic and ionic bonds.

The work of separation for the a-Li_xSi-LiF interface is listed in Fig. 1c and shows the corresponding concentration. As the Li concentration increases, the work of separation increases from 0.21 J m⁻² (the a-Li_{3.75}Si-LiF interface) to 0.26 J m⁻² (the a-Li_{0.25}Si-LiF interface). However, the work of separation is much smaller than the a-LiSi-Cu interface reported by Shenoy and co-workers (1.55 J m⁻²) (ref. 51).

MD simulation methodology. MD simulations were performed using a many-body polarizable APPLE&P force field. The APPLE&P force-field functional form is described in detail elsewhere^{27,29,52}; main features of the force field are briefly discussed here. Electrostatic interactions are described using permanent charges that are centred on atoms. Off-atom-situated partial charges are also added on the ether oxygens in C-O-C and the N atoms of the TFSI⁻ anion to improve the electrostatic potential description around these species. The atom-centred isotropic dipole polarizability is used to represent the induced dipoles that are damped using Thole formalism with the screening parameter ($a_i = 0.4$). The repulsion-dispersion interactions were modelled using a Buckingham potential. Combining rules developed in a previous work⁵², we applied them to the Buckingham potential for cross-terms for all atom pairs with, the exception of interactions with the Li⁺ cation. The TFSI⁻ and Li⁺ force-field parameters are taken from Suo et al.²⁷, the ether, Li and TFSI⁻ parameters are taken from Alvarado et al.⁵³ and the THF and MTHF charges and bonded parameters were developed in this work by fitting partial charges to the electrostatic potential around molecules obtained using the Møller-Plesset perturbation theory second-order MP2 with the aug-cc-pvTz basis set⁵⁴.

The MD simulation package WMI-MD was used for all the MD simulations. The Ewald summation method was used for the electrostatic interactions between the permanent charges with either permanent charges or induced dipole moments with $k=6^3$ vectors. Following previous work⁵⁵, multiple timestep integration was employed with an inner timestep of 0.5 fs (bonded interactions), a central time step of 1.5 fs for all non-bonded interactions within a truncation distance of 8.0 Å and an outer timestep of 3.0 fs for all non-bonded interactions between 7.0 Å and the non-bonded truncation distance of 14–16 Å. The reciprocal part of Ewald was calculated every 3.0 fs. A Nose-Hoover thermostat and a barostat were used to control the temperature and pressure with the associated frequencies of 10⁻² and 0.1 × 10⁻⁴ fs. The atomic coordinates were saved every 2 ps for postanalysis.

Initial equilibration runs of ~6 ns were performed in an NPT ensemble to obtain the equilibrium box size that is used in the follow-up equilibration and production runs performed in the NVT ensemble. The composition of each MD simulation cell is given in Table 2 along with the length of equilibration and production runs. Rounded values of molarity were used in the discussion of the MD simulation results. Ionic conductivity was extracted with a previously described methodology⁵⁶ and is reported in Table 2.

Additional MD simulations were performed on pure THF and MTHF solvents and their mixture THF-MTHF (1:1 v/v) to validate the ability of the developed force field to predict thermodynamic and transport properties, as shown in Table 1. Viscosity and self-diffusion coefficients were extracted from the MD simulations using the Einstein relation⁵². Self-diffusion coefficients were corrected for the finite-size effects, as previously discussed⁵². Dielectric constants were calculated from fluctuations of the mean-squared dipole moment of the simulation box following the approach of Neumann and Steinhäuser⁵⁷ and also summarized in Table 1.

Calculations of electrolyte reduction. The reduction energy (E_{red}) and free energy (G_{red}) of a complex (M) relative to the Li/Li⁺ scale is defined using the thermodynamic energy cycles and is given by equations (1) and (2)^{58,59}:

$$E_{\text{red}}(\text{M}) = -[\Delta E_{\text{a}} + \Delta G_{\text{S}}^0(\text{M}^-) - \Delta G_{\text{S}}^0(\text{M})]/F - 1.4 \quad (1)$$

$$G_{\text{red}}(\text{M}) = -[\Delta G_{\text{a}} + \Delta G_{\text{S}}^0(\text{M}^-) - \Delta G_{\text{S}}^0(\text{M})]F - 1.4 \quad (2)$$

where ΔE_{a} and ΔG_{a} are the electron attachment energy at 0 K and free energy in the gas phase at 298.15 K, respectively, $\Delta G_{\text{S}}^0(\text{M}^-)$ and $\Delta G_{\text{S}}^0(\text{M})$ are the free energies of solvation of the reduced and initial complexes, respectively, and F is the Faraday constant. A shift factor of 1.4 accounts for the difference between the absolute potential scale and Li/Li⁺. The shift factor depends on the nature of solvent, salt and concentration, and might vary by 0.1–0.3 V due to the variation of the Li free energy of solvation in various solvents^{58,60}.

QC calculations were performed using g16 Gaussian software, revision C⁶¹. Solvation energy was calculated using the polarized continuum model with THF parameters for the ether-containing solvates and acetone parameters with a dielectric constant of $\epsilon = 20$ for LiPF₆-EC-DMC clusters. A more accurate but computationally expensive composite G4MP2 methodology was used to predict the energy and free energy of the smaller clusters. DFT calculations using the B3LYP functional with the 6–31+G(d,p) basis set were used to predict the reduction stability for the larger clusters after confirming that the B3LYP/6–31+G(d,p) calculations predicted the reduction energy and free energy for the smaller solvates in good agreement with the more accurate and reliable G4MP2 calculations, as shown in Supplementary Fig. 4. When reduction of the TFSI⁻ anion was coupled with its decomposition (S–N, S–C or C–F bond breaking) or P–F bond breaking in (LiPF₆)₂ B3LYP/6–31+G(d,p), DFT overestimated their reduction potential compared with the G4MP2 results, as shown in Supplementary Fig. 3.

Data availability

The authors declare that the data supporting the findings of this study are available within the article and its Supplementary Information files.

Received: 23 July 2019; Accepted: 9 March 2020;

Published online: 20 April 2020

References

- Li, J. & Dahn, J. An in situ X-ray diffraction study of the reaction of Li with crystalline Si. *J. Electrochem. Soc.* **154**, A156–A161 (2007).
- Kasavajjula, U., Wang, C. & Appleby, A. J. Nano- and bulk-silicon-based insertion anodes for lithium-ion secondary cells. *J. Power Sources* **163**, 1003–1039 (2007).

3. Chen, Z., Chevrier, V., Christensen, L. & Dahn, J. Design of amorphous alloy electrodes for Li-ion batteries a big challenge. *Electrochem. Solid State Lett.* **7**, A310–A314 (2004).
4. Liu, W.-R. et al. Effect of electrode structure on performance of Si anode in Li-ion batteries: Si particle size and conductive additive. *J. Power Sources* **140**, 139–144 (2005).
5. Obrovac, M. & Krause, L. Reversible cycling of crystalline silicon powder. *J. Electrochem. Soc.* **154**, A103–A108 (2007).
6. Kim, H., Seo, M., Park, M. H. & Cho, J. A critical size of silicon nano-anodes for lithium rechargeable batteries. *Angew. Chem. Int. Ed.* **49**, 2146–2149 (2010).
7. Liu, X. H. et al. Anisotropic swelling and fracture of silicon nanowires during lithiation. *Nano Lett.* **11**, 3312–3318 (2011).
8. Chan, C. K. et al. in *Materials for Sustainable Energy: A Collection of Peer-Reviewed Research and Review Articles from Nature Publishing Group* (ed. Dusastre, V.) 187–191 (World Scientific, 2011).
9. Cui, L.-F., Ruffo, R., Chan, C. K., Peng, H. & Cui, Y. Crystalline-amorphous core-shell silicon nanowires for high capacity and high current battery electrodes. *Nano Lett.* **9**, 491–495 (2008).
10. Li, S. et al. High-rate aluminium yolk-shell nanoparticle anode for Li-ion battery with long cycle life and ultrahigh capacity. *Nat. Commun.* **6**, 7872 (2015).
11. Yao, Y. et al. Interconnected silicon hollow nanospheres for lithium-ion battery anodes with long cycle life. *Nano Lett.* **11**, 2949–2954 (2011).
12. Park, M.-H. et al. Silicon nanotube battery anodes. *Nano Lett.* **9**, 3844–3847 (2009).
13. Lu, Z. et al. Nonfilling carbon coating of porous silicon micrometer-sized particles for high-performance lithium battery anodes. *ACS Nano* **9**, 2540–2547 (2015).
14. Magasinski, A. et al. High-performance lithium-ion anodes using a hierarchical bottom-up approach. *Nat. Mater.* **9**, 353–358 (2010).
15. Son, I. H. et al. Silicon carbide-free graphene growth on silicon for lithium-ion battery with high volumetric energy density. *Nat. Commun.* **6**, 8393 (2015).
16. Zhang, C. J. et al. High capacity silicon anodes enabled by MXene viscous aqueous ink. *Nat. Commun.* **10**, 849 (2019).
17. Wang, C. et al. Self-healing chemistry enables the stable operation of silicon microparticle anodes for high-energy lithium-ion batteries. *Nat. Chem.* **5**, 1042–1048 (2013).
18. Choi, S., Kwon, T.-w., Coskun, A. & Choi, J. W. Highly elastic binders integrating polyrotaxanes for silicon microparticle anodes in lithium ion batteries. *Science* **357**, 279–283 (2017).
19. Xu, Z. et al. Silicon microparticle anodes with self-healing multiple network binder. *Joule* **2**, 950–961 (2018).
20. Kovalenko, I. et al. A major constituent of brown algae for use in high-capacity Li-ion batteries. *Science* **334**, 75–79 (2011).
21. Li, Y. et al. Growth of conformal graphene cages on micrometre-sized silicon particles as stable battery anodes. *Nat. Energy* **1**, 15029 (2016).
22. Peled, E. & Menkin, S. SEI: past, present and future. *J. Electrochem. Soc.* **164**, A1703–A1719 (2017).
23. Sina, M. et al. Direct visualization of the solid electrolyte interphase and its effects on silicon electrochemical performance. *Adv. Mater. Interfaces* **3**, 1600438 (2016).
24. Michan, A. L. et al. Solid electrolyte interphase growth and capacity loss in silicon electrodes. *J. Am. Chem. Soc.* **138**, 7918–7931 (2016).
25. Jin, Y. et al. Understanding fluoroethylene carbonate and vinylene carbonate based electrolytes for Si anodes in lithium ion batteries with NMR spectroscopy. *J. Am. Chem. Soc.* **140**, 9854–9867 (2018).
26. Vogl, U. S. et al. The mechanism of SEI formation on a single crystal Si(100) electrode. *J. Electrochem. Soc.* **162**, A603–A607 (2015).
27. Suo, L. et al. 'Water-in-salt' electrolyte enables high-voltage aqueous lithium-ion chemistries. *Science* **350**, 938–943 (2015).
28. Borodin, O. Challenges with prediction of battery electrolyte electrochemical stability window and guiding the electrode-electrolyte stabilization. *Curr. Opin. Electrochem.* **13**, 86–93 (2019).
29. Suo, L. et al. Advanced high-voltage aqueous lithium-ion battery enabled by 'water-in-bisalt' electrolyte. *Angew. Chem. Int. Ed.* **55**, 7136–7141 (2016).
30. Zheng, J. et al. 3D visualization of inhomogeneous multi-layered structure and Young's modulus of the solid electrolyte interphase (SEI) on silicon anodes for lithium ion batteries. *Phys. Chem. Chem. Phys.* **16**, 13229–13238 (2014).
31. Hall, D. S., Self, J. & Dahn, J. R. Dielectric constants for quantum chemistry and Li-ion batteries: solvent blends of ethylene carbonate and ethyl methyl carbonate. *J. Phys. Chem. C* **119**, 22322–22330 (2015).
32. Jiao, S. et al. Stable cycling of high-voltage lithium metal batteries in ether electrolytes. *Nat. Energy* **3**, 739–746 (2018).
33. Ren, X. et al. High-concentration ether electrolytes for stable high-voltage lithium metal batteries. *ACS Energy Lett.* **4**, 896–902 (2019).
34. Chan, C. K., Ruffo, R., Hong, S. S. & Cui, Y. Surface chemistry and morphology of the solid electrolyte interphase on silicon nanowire lithium-ion battery anodes. *J. Power Sources* **189**, 1132–1140 (2009).
35. Yoon, T., Chapman, N., Seo, D. M. & Lucht, B. L. Lithium salt effects on silicon electrode performance and solid electrolyte interphase (SEI) structure, role of solution structure on SEI formation. *J. Electrochem. Soc.* **164**, A2082–A2088 (2017).
36. Chang, X. et al. Enabling high performance lithium storage in aluminum: the double edged surface oxide. *Nano Energy* **41**, 731–737 (2017).
37. Ridgway, P. et al. Comparison of cycling performance of lithium ion cell anode graphites. *J. Electrochem. Soc.* **159**, A520–A524 (2012).
38. Wang, X. et al. High damage tolerance of electrochemically lithiated silicon. *Nat. Commun.* **6**, 8417 (2015).
39. Park, M. S. et al. A highly reversible lithium metal anode. *Sci. Rep.* **4**, 3815 (2014).
40. Boniface, M. et al. Nanoscale chemical evolution of silicon negative electrodes characterized by low-loss STEM-EELS. *Nano Lett.* **16**, 7381–7388 (2016).
41. Danet, J., Brousse, T., Rasim, K., Guyomard, D. & Moreau, P. Valence electron energy-loss spectroscopy of silicon negative electrodes for lithium batteries. *Phys. Chem. Chem. Phys.* **12**, 220–226 (2010).
42. Zhang, Q. et al. Synergetic effects of inorganic components in solid electrolyte interphase on high cycle efficiency of lithium ion batteries. *Nano Lett.* **16**, 2011–2016 (2016).
43. Bedrov, D., Borodin, O. & Hooper, J. B. Li⁺ transport and mechanical properties of model solid electrolyte interphases (SEI): insight from atomistic molecular dynamics simulations. *J. Phys. Chem. C* **121**, 16098–16109 (2017).
44. Wang, X., Li, Y. & Meng, Y. S. Cryogenic electron microscopy for characterizing and diagnosing batteries. *Joule* **2**, 2225–2234 (2018).
45. Hohenberg, P. & Kohn, W. Inhomogeneous electron gas. *Phys. Rev.* **136**, B864 (1964).
46. Kohn, W. & Sham, L. J. Self-consistent equations including exchange and correlation effects. *Phys. Rev.* **140**, A1133 (1965).
47. Kresse, G. & Hafner, J. Ab initio molecular dynamics for liquid metals. *Phys. Rev. B* **47**, 558 (1993).
48. Blöchl, P. E. Projector augmented-wave method. *Phys. Rev. B* **50**, 17953 (1994).
49. Perdew, J. P., Burke, K. & Ernzerhof, M. Generalized gradient approximation made simple. *Phys. Rev. Lett.* **77**, 3865–3868 (1996).
50. Kresse, G. & Furthmüller, J. Efficient iterative schemes for ab initio total-energy calculations using a plane-wave basis set. *Phys. Rev. B* **54**, 11169–11186 (1996).
51. Stournara, M. E. et al. Li segregation induces structure and strength changes at the amorphous Si/Cu interface. *Nano Lett.* **13**, 4759–4768 (2013).
52. Borodin, O. Polarizable force field development and molecular dynamics simulations of ionic liquids. *J. Phys. Chem. B* **113**, 11463–11478 (2009).
53. Alvarado, J. et al. Bisalt ether electrolytes: a pathway towards lithium metal batteries with Ni-rich cathodes. *Ener. Env. Sci.* **12**, 780–794 (2019).
54. Yang, Y. et al. High-efficiency lithium-metal anode enabled by liquefied gas electrolytes. *Joule* **3**, 1986–2000 (2019).
55. Borodin, O. et al. Insights into the structure and transport of the lithium, sodium, magnesium, and zinc bis(trifluoromethanesulfonyl) imide salts in ionic liquids. *J. Phys. Chem. C* **122**, 20108–20121 (2018).
56. Borodin, O. & Smith, G. D. Quantum chemistry and molecular dynamics simulation study of dimethyl carbonate: ethylene carbonate electrolytes doped with LiPF₆. *J. Phys. Chem. B* **113**, 1763–1776 (2009).
57. Neumann, M. & Steinhauser, O. Computer simulation and the dielectric constant of polarizable polar systems. *Chem. Phys. Lett.* **106**, 563–569 (1984).
58. Giner, B., Gascón, I., Villares, A., Cea, P. & Lafuente, C. Densities and viscosities of the binary mixtures of tetrahydrofuran with isomeric chlorobutanes at 298.15 K and 313.15 K. *J. Chem. Eng. Data* **51**, 1321–1325 (2006).
59. Vallés, C., Pérez, E., Mainar, A. M., Santafé, J. & Domínguez, M. Excess enthalpy, density, speed of sound, and viscosity for 2-methyltetrahydrofuran + 1-butanol at (283.15, 298.15, and 313.15) K. *J. Chem. Eng. Data* **51**, 1105–1109 (2006).
60. Hayamizu, K., Aihara, Y., Arai, S. & Martinez, C. G. Pulse-gradient spin-echo H-1, Li-7, and F-19 NMR diffusion and ionic conductivity measurements of 14 organic electrolytes containing LiN(SO₂CF₃)₂. *J. Phys. Chem. B* **103**, 519–524 (1999).
61. Haines, W. M. & Lide, D. R. *CRC Handbook of Chemistry and Physics* 2012–2013 93rd edn (CRC, 2012).
62. Delsignore, M., Maaser, H. E. & Petrucci, S. Molecular relaxation of lithium salts in 2-methyltetrahydrofuran at 25°C. *J. Phys. Chem.* **88**, 2405–2411 (1984).
63. Borodin, O., Behl, W. & Jow, T. R. Oxidative stability and initial decomposition reactions of carbonate, sulfone, and alkyl phosphate-based electrolytes. *J. Phys. Chem. C* **117**, 8661–8682 (2013).
64. Fry, A. J. Computational applications in organic electrochemistry. *Curr. Opin. Electrochem.* **2**, 67–75 (2017).
65. Jow, T. R., Xu, K., Borodin, O. & Ue, M. *Electrolytes for Lithium and Lithium-Ion Batteries* Vol. 58 (Springer, 2014).
66. Frisch, M. J. T. et al. Gaussian 09 (Gaussian Inc., 2016).

Acknowledgements

This project was supported by the Department of Energy (DOE) Office of Energy Efficiency and Renewable Energy (EERE) through Battery500 Consortium under contract no. DE-EE0008202. Cryo-EM work was performed at the Center for Functional Nanomaterials, which is a US DOE Office of Science User Facility at Brookhaven National Laboratory, under Contract no. DE-SC0012704. Modelling work at the Army Research Laboratory (ARL) by O.B. was supported by ARL Enterprise for Multiscale Modeling. The authors acknowledge helpful discussions with M. Schroeder (ARL) and T. Pollard (ARL).

Author contributions

J.C., X.F. and Q.L. contributed equally to this work. J.C., X.F. and C.W. conceived the idea for the project. J.C., X.F. and Q.L. prepared the materials and performed the electrochemical experiments. O.B. and X.J. conducted the QC calculations and MD simulations. M.R.K. and H.H. conducted the electrochemical AFM measurements. S.H., D.S., Y.X. and C.W. performed the cryo-TEM measurements. H.Y. and E.G. obtained the

LiF spatial distribution and EELS spectra. L.C. and C.Y. coated the electrodes. All the authors discussed the results, analysed the data and drafted the manuscript.

Competing interests

A US patent with the provisional application number 62/978637 has been filed.

Additional information

Supplementary information is available for this paper at <https://doi.org/10.1038/s41560-020-0601-1>.

Correspondence and requests for materials should be addressed to O.B. or C.W.

Reprints and permissions information is available at www.nature.com/reprints.

Publisher's note Springer Nature remains neutral with regard to jurisdictional claims in published maps and institutional affiliations.

© The Author(s), under exclusive licence to Springer Nature Limited 2020